Dynamics of Transient Hole Doping in Epitaxial Graphene

Swapnil M. Mhatre[1,2], Ngoc Thanh Mai Tran[1,3], Heather M. Hill[1], Dipanjan Saha[1], Angela R. Hight Walker[1], Chi-Te Liang[2], Randolph E. Elmquist[1], David B. Newell[1], and Albert F. Rigosi[1*]

[1]*Physical Measurement Laboratory, National Institute of Standards and Technology (NIST), Gaithersburg, MD 20899, United States*

[2]*Graduate Institute of Applied Physics, National Taiwan University, Taipei 10617, Taiwan*

[3]*Joint Quantum Institute, University of Maryland, College Park, Maryland 20742, United States*

(Received 22 March 2022;)

ABSTRACT: This work reports the dynamics of transient hole doping in epitaxial graphene devices by using nitric acid as an adsorbent. The timescales associated with corresponding desorption processes are extracted from the data. The understanding of reversible hole doping without gating is of crucial importance to those fabricating devices with a particular functionality. Measurements of the electrical and optical properties of several devices post-exposure were performed with transport temperatures between 300 K and 1.5 K. Ambient conditions are applied to non-transport measurements to replicate the most likely laboratory conditions for handling devices using this doping method. The relevant timescales from transport measurements are compared with results from Raman spectroscopy measurements.

* Email: albert.rigosi@nist.gov

I. INTRODUCTION

Graphene continues to attract attention for its desirable electrical properties [1-4]. Though it can be synthesized in multiple ways, graphene grown epitaxially (EG) has been shown to harbor a specific set of advantages, namely its growth scale and ability to exhibit a robust quantum Hall effect [5-9]. For applications that require both of these advantages, like resistance metrology [10-11], a more restricted parameter space is immediately imposed due to the difficulty of fabricating suitable gates. For instance, EG that has been grown on large scales exhibits carrier densities that are difficult to control and has thus been subject to alternate forms of gating and doping that do not require a metallic top or bottom gate [12-14]. The application space would expand if the carrier density could be controlled over a large lateral range to fully take advantage of the types of devices into which EG may be fabricated.

In this work, the dynamics behind hole doping in EG are examined by using nitric acid as an adsorbent. Though there is some work already pertaining to this particular interaction [15-17], some elements, such as timescales associated with the nitric acid constituent desorption process, have not yet been fully understood. Further characterization of these processes is important for any two-dimensional (2D) material intended for devices with a particular functionality, such as devices exhibiting photovoltaic properties [18-19], charge density waves [20-21], or *p-n* junctions [22-27]. Furthermore, the large-scale gating that becomes enabled from the understanding of these processes can also be directly applicable to photodetection [28-32] and electron optics [33-35].

Specifically, a focus is placed on quantum transport data taken at low (1.5 K) and room temperatures. A main objective for electrical measurements was to monitor the properties of a

device post-exposure, with the intention of obtaining information about the timescales associated with desorption. Measurements were performed under ambient conditions to replicate the most likely situation for handling devices using this doping method. Raman spectroscopy is also employed with the main objective of comparing the relevant timescales determined from transport measurements with those from the devices' optical properties. A discussion surrounding a suitable Langmuir model supports the observations made and allows one to gain insights on how to interpret the several time constants in the data.

II. EXPERIMENTAL AND NUMERICAL METHODS

A. Sample Preparation

EG films were grown on 4H-SiC substrates by the high-temperature sublimation method, which allows carbon atoms on the surface to restructure into a hexagonal lattice [36]. Chips were diced from 4H-SiC(0001) wafers from CREE (see Acknowledgments), cleaned with a 5:1 diluted solution of hydrofluoric acid and deionized water, and coated with a dilute solution of the resist AZ 5214E in isopropyl alcohol to use the benefits of polymer-assisted sublimation growth (PASG) [37]. The chemically smoothed Si-face of each chip was placed on a polished glassy carbon slab (SPI Glas 22, see Acknowledgments) to limit the escape rate of the Si atoms, thereby improving graphene homogeneity. The graphite-lined resistive-element furnace (Materials Research Furnaces Inc., see Acknowledgments) was flushed with argon gas and filled to about 103 kPa from a 99.999 % liquid argon source. During growth, the furnace was held at 1900 °C for between 4 min to 5 min, with heating and cooling rates of about 1.5 °C/s.

As-grown EG films had their uniformity verified by means of confocal laser scanning microscopy (CLSM) and optical microscopy. Device fabrication closely followed steps

described in other work and generally included a gold protection layer, photolithography processes, and protection layer removal [38-39]. For some devices, superconducting NbTiN was deposited as the electrical contact material as an alternate means to determine possible differences in contrast with gold contacts [40], of which none were observed. The final fabrication step for devices that did not serve as the control was to undergo a functionalization process for regulating the carrier density without the need for a top gate. The functional group $Cr(CO)_3$ was implemented in a similar manner to previous studies [13, 41].

The carrier density of these functionalized EG devices following exposure to air for about one day is on the order 10^{10} cm^{-2} [13], and this behavior of a functionalized device to asymptotically approach the Dirac point provides a valuable comparison to the control devices, especially since the typical value of electron doping in EG can be as high as of 10^{13} cm^{-2}, in part due to the buffer layer beneath the EG layer [42-43]. A set of final device images are shown in Fig. 1 (a)-(b). First, an optical image of a finished, functionalized device is shown after wire bonding. One may notice spots within the device perimeter, which are small clusters of oxidized chromium with virtually no interaction with the EG layer [13]. A control device is shown in Fig. 1 (b), with a small blue box indicating the region where an example CLSM image was captured. This capture can be seen in Fig. 1 (d) and verifies the homogeneous growth quality of the EG. A comparison can be made with an example of an undergrown EG film in the preceding panel (Fig. 1 (c), showing material that would not be used for device fabrication).

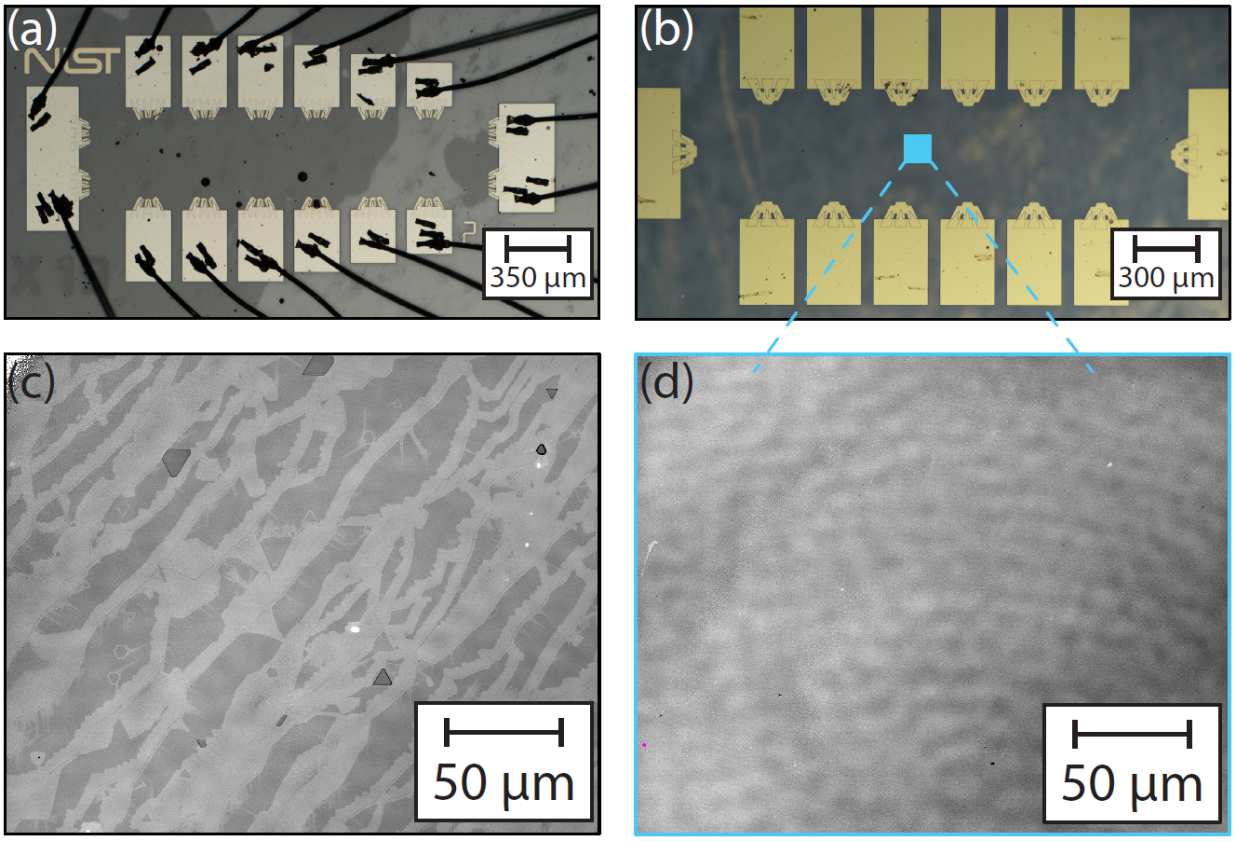

FIG. 1. (Color online) Graphene material and device quality. (a) An optical microscope image of a functionalized device is shown after wire bonding. Spots within the device perimeter are clusters of oxidized chromium that do not interact with the EG layer beneath. (b) An optical image of a standard device is shown. The small blue box indicates a region within which a closer inspection was performed to verify growth quality. (c) Confocal laser scanning microscopy was utilized to capture example images of undergrown EG on SiC to compare with (d). (d) An example CLSM image is shown to verify the homogeneous growth quality of the EG and is the relevant standard by which all grown material is compared.

B. Exposure and Electrical Transport

For quantum Hall transport measurements, a Janis Cryogenics system was used (see Acknowledgments). All data were collected at temperatures of 1.5 K and magnetic fields between -9 T and 9 T, primarily to determine the initial hole doping of each device. All samples

were consistently exposed to nitric acid vapors in a standard fume hood, with each exposure taking place 3 cm from the surface of the liquid for a duration of 2 min. The duration was selected based on the reported faster timescales for NO_3 adsorption on EG [16]. Traditional lock-in measurement techniques were used for evaluating the longitudinal (R_{xx}) resistances for each device, and all source-drain currents were set to 1 μA.

C. Raman Spectroscopy

Raman spectroscopy was used to both confirm the presence of a homogeneous EG layer as well as to monitor the 2D (G') mode. These measurements were performed with a Renishaw InVia micro-Raman spectrometer (see Acknowledgments) using a 633 nm wavelength excitation laser source. All spectra were measured and collected using a backscattering configuration, 2 μm spot size, 300 s acquisition time, 1.7 mW power, 50 × objective, and 1200 mm^{-1} grating. In the case of confirming the quality, rectangular Raman maps were collected with step sizes of 20 μm in a 5 by 3 raster-style grid. For time-dependent Raman measurements, several sets of data were collected on single points on the film post-exposure with a 30 s delay between measurements.

III. TRANSPORT AND TRANSIENT DOPING

The challenge of meeting the objectives of this work stems mostly from the necessity of determining a room temperature phenomenon based on electrical properties that require magnetic fields and, in some instances, cryogenic temperatures. More specifically, room temperature desorption timescales can be most easily determined by knowing the time dependence of the hole density (n_h) after exposure. This makes the most physical sense since the number of carriers is roughly correlated with the number of adsorbates, or lack thereof. Two

issues thus arise: (1) measurement of n_h requires a reliable magnetic field and is most frequently available as a cryogenically cooled electromagnet, typically accompanied by a sample space that is in close physical and thermal proximity to that magnet, and (2) the rate of change of n_h is typically temperature dependent [13], meaning that room temperature timescales cannot be measured in an environment with unreliable temperature stability. Though one can use a sample heater to ensure a 300 K bath near the device, the size of the devices (cm scale) would likely render this procedure unreliable since providing evidence of temperature uniformity on that scale is more difficult than simply correlating room temperature resistance behaviors to those seen at cryogenic temperatures.

When doping the control devices, an immediate transport measurement (that is, a device loaded within two minutes of exposure) was made to determine the initial hole density (n_h) at 1.5 K. This cold temperature was used to prevent immediate Fermi level shifting, which would introduce unnecessary error to the data [13]. Additionally, it is important to verify the quality of the resistance plateau should such devices be applied to metrological research, and this can only be done at cold temperatures. Most measurements aside from the initial hole density and plateau quality were performed at room temperature in ambient conditions to replicate laboratory settings. Standard exemplary Hall measurements for a control device can be seen in Fig. 2 (a) as solid black and dashed red curves. An example set of functionalized device measurements are also shown as blue, green, and orange curves of varying dash length. It should be noted that the functionalized devices provide a means of calibration since their hole density is expected to behave predictably [13], with an asymptotic approach to the Dirac point. The slope from each Hall curve at low magnetic fields (less than 1 T) was used for calculating n_h. In Fig. 2 (a), the average initial n_h for the example control and functionalized devices were about 1.6×10^{11} cm^{-2}

and 1.1 × 10^{12} cm^{-2}, respectively. Another electrical measurement involves the monitoring of R_{xx} after exposure to nitric acid vapor for several pairs of longitudinal contact pairs on each of the control devices. A subset of these results is shown in Fig. 2 (b), where all curves come from the same device and the same exposure.

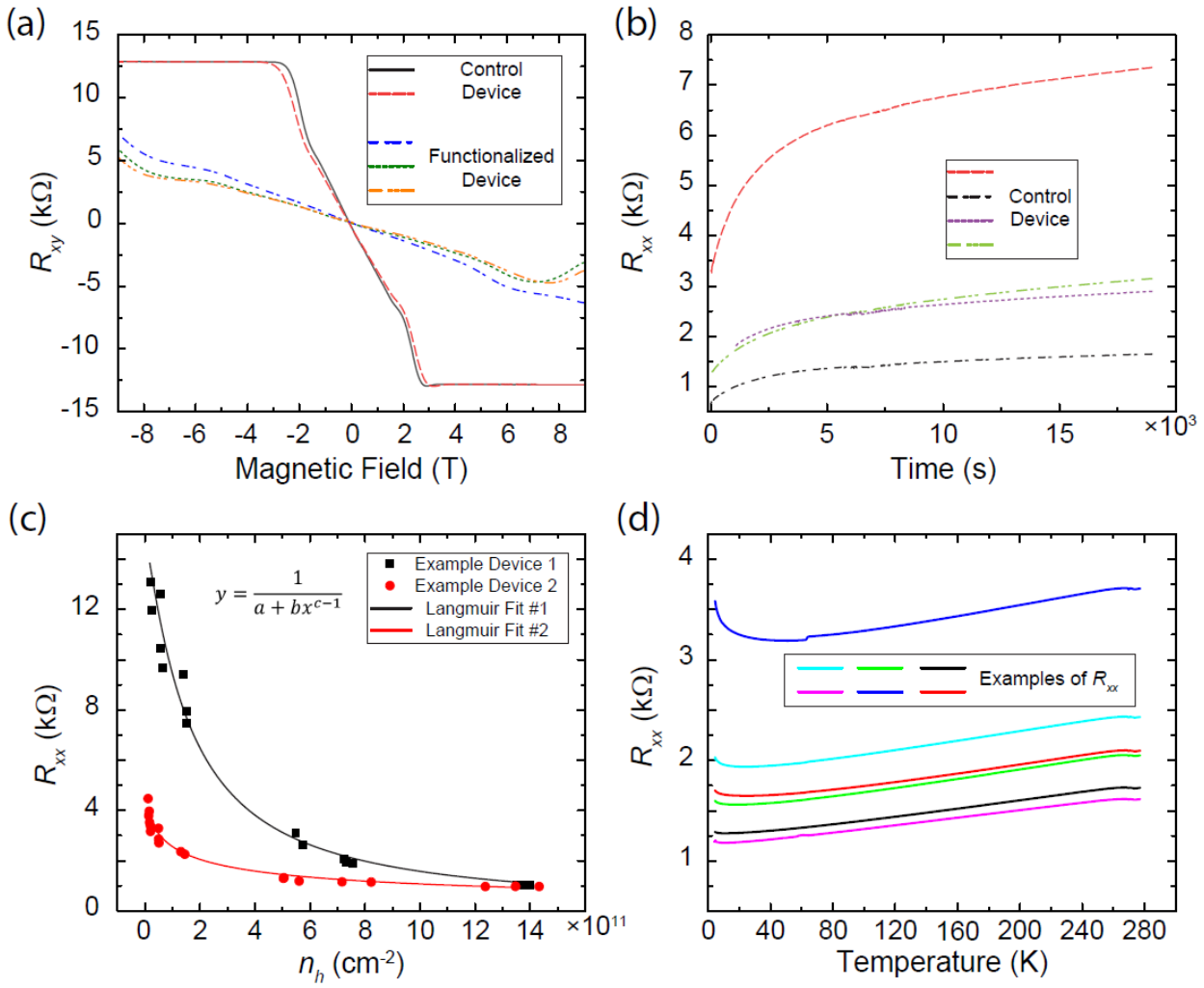

FIG. 2. (Color online) Transport and electrical data. (a) Standard Hall measurements were performed on a control device (solid black and dashed red curves) and a functionalized device (blue, green, and orange curves of varying dash length). The slopes of the Hall curves at low magnetic fields (magnitude less than 1 T) were used to calculate the initial hole densities (n_h) post-exposures. (b) Longitudinal resistances (R_{xx}) for several pairs of longitudinal contact pairs on the control devices were measured after exposure to nitric acid. (c) For two example devices,

measurements are repeated to extract an approximate relationship between R_{xx} and n_h. These relationships are unique to each device. (d) A set of R_{xx} measurements (from a single device) as a function of temperature are shown to support the notion that there is a 1:1 mapping for R_{xx} values between 300 K and 1.5 K. These were collected at six orthogonal pairs from a single device.

The observation that the nominal values of R_{xx} vary significantly stems from the variation in hole density throughout the control device. This behavior is typical and one of the primary reasons that functionalization was sought as a remedy [13]. These treated devices will show more stable and predictable behavior in later figures. Ideally, one would inspect the hole doping as a function of time, as this would reveal more about the desorption processes. Therefore, for every device, low-field determinations of n_h are repeated to extract an approximate relationship between R_{xx} and n_h. For two example control devices, such relationships are plotted in Fig. 2 (c). To transform the time-dependent R_{xx} curve to a time-dependent n_h curve, a characteristic function and suitable fit were necessary. For reasons soon to be described, the ansatz chosen for these fits was based on a Langmuir curve (with a, b, and c as constants):

$$R_{xx} = \frac{1}{a + b{n_h}^{c-1}} \tag{1}$$

The only remaining issue that required attention was the verification that the relationship between a room temperature R_{xx} and a 1.5-K n_h was reasonably a 1:1 correspondence. For instance, not meeting this criterion would imply that one resistance could have two values of n_h, creating inaccuracies in any time-dependent n_h curve. Ergo, as shown in Fig. 2 (d), a set of R_{xx} measurements, all from a single control device, are shown as a function of temperature to support the notion that there is a 1:1 mapping between R_{xx} and n_h values between 300 K and 1.5 K [44].

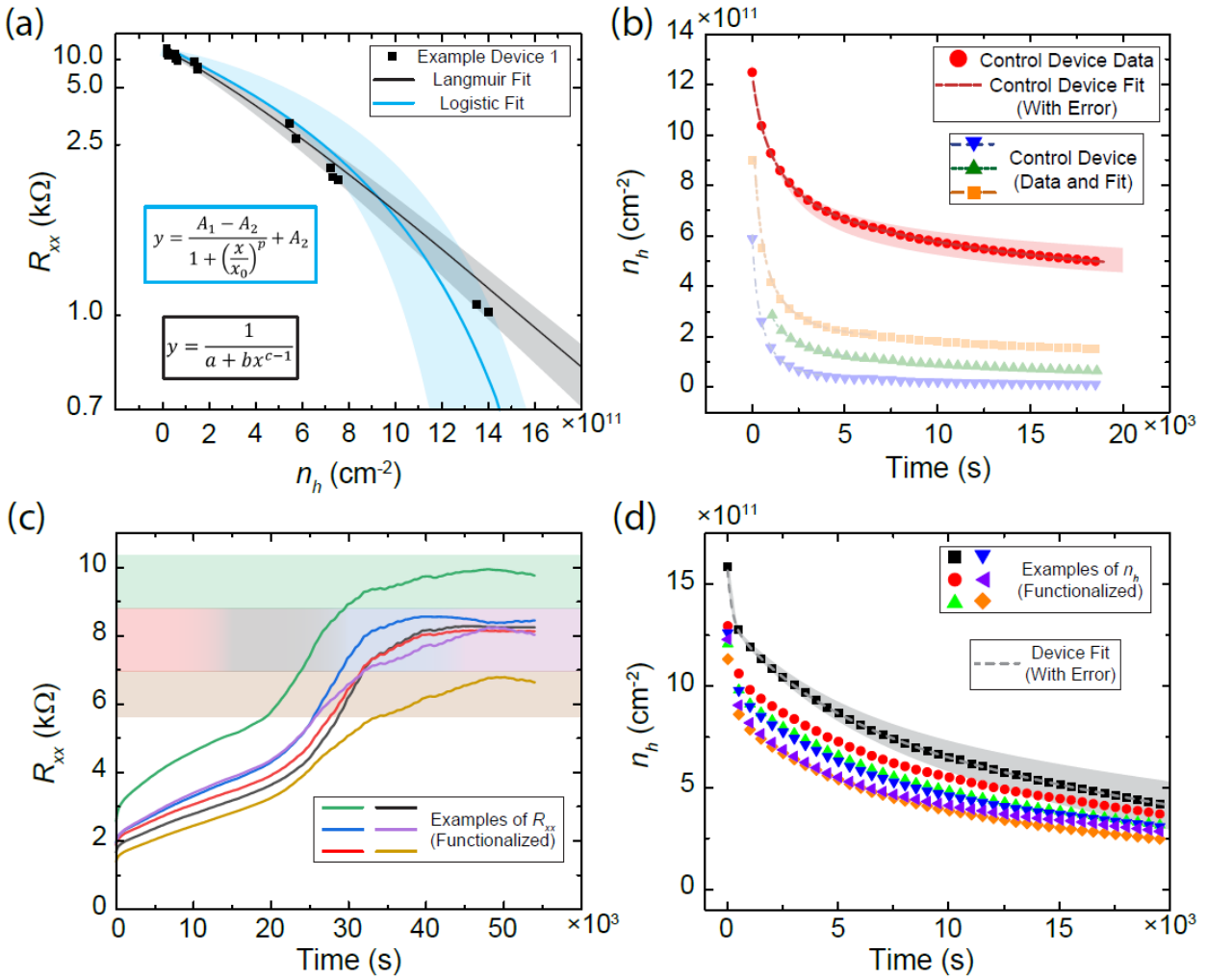

FIG. 3. (Color online) Extracting time constants. (a) An error comparison between a Langmuir fit (black) and a Logistic fit (cyan) reveals that the Langmuir fit is preferred for obtaining the relationship between R_{xx} and n_h. The blue and gray shaded region indicate 1σ error from the fitting procedure. (b) Each Langmuir fit is used to transform the corresponding R_{xx} data to n_h. The shaded region indicates 1σ error from the fitting procedure and is shown only for the top data (red circles) to prevent significant overlap for the other three curves. (c) Example R_{xx} data from functionalized device are shown over a longer duration to emphasize the stabilizing nature of the treatment. Shaded regions are color-matched to the corresponding curves and indicate a region within which the polarity of the charge carrier may change due to the proximity of the Fermi level to the Dirac point. (d) The same data in (c) are transformed to provide a way for extracting time constants that characterize certain doping behaviors. One example fit (and corresponding 1σ error as a shaded region) is shown for the topmost curve.

To justify the use of the Langmuir fit, one may start with the fact that the ideal relationship between the two quantities R_{xx} and n_h is approximately reciprocal [45]. One additional possibility for fitting the data (shown in Fig. 3 (a)) is to use the Logistic fit below (where A_1, A_2, x_0, and p are constants):

$$R_{xx} = \frac{A_1 - A_2}{1 + \left(\frac{n_h}{x_0}\right)^p} + A_2 \tag{2}$$

When considering the errors associated with the fitting procedure (performed with OriginLab, see Acknowledgments), one can compare the adequacy of the fits, as done in Fig. 3 (a) for an example control device. A Langmuir fit (black) and a Logistic fit (cyan) are compared, and from a visual analysis, it became clear that the Langmuir fit would be a better indicator of the relationship between R_{xx} and n_h. Furthermore, an optimal reduced chi-squared validated this determination. The blue and gray shaded region indicate 1σ error from the fitting procedure. The obtained Langmuir fits (as shown in Fig. 3 (b)) were used to transform the corresponding R_{xx} data to n_h. The shaded region indicates 1σ error from the fitting procedure and is shown only for the top data (red circles) to prevent significant overlap for the other three curves. These example curves correspond to Fig. 2 (b).

A similar transformation can be performed for data acquired with functionalized devices. For instance, an example set of R_{xx} data are shown in Fig. 3 (c) over a longer duration to emphasize the asymptotic behavior induced by the treatment. The shaded regions are color-matched to their corresponding curves to show the approximate range of longitudinal resistances within which the polarity of the charge carrier is expected to change indiscriminately due to the proximity of the

Fermi level to the Dirac point. The final transformed example data are then shown in Fig. 3 (d) to demonstrate both that functionalized devices have a smaller variation of hole density across the device and that similar time constants can be extracted. One example fit is shown in dashed gray (with a shaded gray region corresponding to a 1σ fitting error). An additional note to make is that functionalized devices consistently started at the same initial n_h after exposure (to within parts in 10^{10} cm^{-2}), providing a more predictable doping process than their control counterparts, with an initial n_h varying by, at most, a few parts in 10^{11} cm^{-2}.

All the data in Fig. 3 (d) were then fitted with three-term exponential decays to account for several expected desorbed species of molecule (*i.e.* NO_3, NO_2, and water from potential dissociation of HNO_3 that has physisorbed on the EG surface) [16]. Three-term decays provided an optimized reduced chi-squared when compared to double- or single-term decays (see next section). The three time constants (τ_1, τ_2, and τ_3) averaged from all the fits corresponding to the data are 204 s ± 95 s, 2575 s ± 326 s, and 7.35×10^4 s ± 2.43×10^4 s, respectively. There were no significant differences between the control and functionalized devices. To fully understand these constants, more analysis and discussion on Langmuir modeling is required (not to be confused with the previously described Langmuir fit needed for the transformation between R_{xx} and n_h).

IV. LANGMUIR MODELING AND RAMAN MONITORING

A. Three-Species Langmuir Model

The interpretation of these time constants required further analysis. If it is assumed that adsorbents have saturated the EG surface after the exposure, this analysis becomes more straightforward for short monitoring times. Some work discussing NO_2 adsorption on EG show

that the associated time constants for this molecule are on the order of 100 s [47-48]. This description fits well within the extracted value of τ_1. Combined with the reports that the adsorption of oxygen and water on graphene takes place on the order of 2 h [49-53], there should not be any immediate competing effects at such short timescales. The longest timescale (τ_3) may be compared with a very similar value obtained from a previous work that described the time constant as representing the desorption of water from the EG surface (that value was reported to be approximately 7×10^4 s) [13]. This leaves the remaining component of the nitric acid byproducts, NO_3, to be described by τ_2. More information on the interactions of the various molecules is provided in the Supplemental Material [46].

Though it was shown that water was the dominant contributor to desorption when competing with oxygen [13], it cannot be immediately assumed for a three species competition at longer times (long enough to neglect contributions from NO_2). Though a two species Langmuir model has been shown in the literature [54], a model for three competing species has not. To develop this model, three ordinary differential equations were set up that describe the occupancies of oxygen, water, and NO_3 on EG sites [54]:

$$\frac{d\theta_{i,j,k}}{dt} = k_{i,j,k(A)} p_{i,j,k}\left(1 - \theta_i(t) - \theta_j(t) - \theta_k(t)\right) - k_{i,j,k(D)}\theta_{i,j,k}(t) \tag{3}$$

Here, i, j, and k represent each of the three competing species. In all cases, $k_{(A)}$ and $k_{(D)}$ are adsorption and desorption rate constants, respectively. Rate constants take on the form: $k_{A,D} = \nu\, exp\left[\frac{-E_{ads,des}}{k_B T}\right]$, with E_{ads} and E_{des} as the adsorption and desorption energy per molecule, respectively, ν is the attempt frequency (typically approximated as 10^{13} s^{-1} [13]), k_B is the

Boltzmann constant, and T is temperature (K). The term $P_{(LD)}$ denotes the Langmuir desorption pressure, unique to each of the gas species, with the form:

$$P_{LD} = \frac{k_B T}{\left(\frac{h^2}{2\pi m k_B T}\right)^{3/2}} \tag{4}$$

The listed quantities in all equations should be converted to SI units (or remain unitless) to avoid unit confusion within the expressions. In Eq. 4, h is the Planck constant, and m is the mass of a single molecule of one of the gas species (kg). Combining all of these elements with Eq. 3 allows one to solve for equilibrium occupancies, where the steady state solutions may be written as [54]:

$$\theta_{i,j,k} = \frac{p_{i,j,k}}{p_{i,j,k} + P_{i,j,k\,(LD)} exp\left[\frac{-E_{i,j,k}}{k_B T}\right]\left[1 + \frac{p_{j,k,i}}{P_{j,k,i\,(LD)}} exp\left[\frac{E_{j,k,i}}{k_B T}\right] + \frac{p_{k,i,j}}{P_{k,i,j\,(LD)}} exp\left[\frac{E_{k,i,j}}{k_B T}\right]\right]} \tag{5}$$

In Eq. 5, p is the partial pressure (with the fractional form multiplied by the total pressure) of the gas species, which is about 0.209 for oxygen and 0.00916 for water at room temperature and 40 % relative humidity under normal ambient conditions. The net adsorption energy E is 0.15 eV and 0.1 eV for oxygen and water, respectively [50-51]. An estimate of the partial pressure for NO_3 is needed to obtain occupancy information. This can be done using Fick's laws of diffusion along with the conditions that there are no significant air currents (as is the case for the used probe, whose sample holder resides within a metallic encasement). The mean squared

displacement may be estimated as $6Dt$, where t is the time spent diffusing and D is the diffusion coefficient, which may be approximated as 10^{-5} m^2/s [55]. The condition is that a saturated sample may have most of its sites occupied, and for a 1 cm^2 area, this would amount to about 10^{15} cm^{-2} molecules.

With these conditions, the square root of the mean squared displacement can be calculated to get approximate distances of 1 cm, 25 cm, and 75 cm for the corresponding example times of t_α = 200 s, t_β = 1000 s, and t_γ = 8000 s, respectively, after the exposure. These times were selected to avoid any dominant transient effects from NO_2. Spreading these molecules out from the surface of EG to the volume of diffusion yields the following three unitless partial pressures: $p_\alpha = 10^{-4}$, $p_\beta = 4 \times 10^{-6}$, and $p_\gamma = 1.33 \times 10^{-6}$. The final element needed is net adsorption energy, which can be approximated by the rate constant formula after Eq. 3. By inverting τ_{NO_3} ($E_{des} \approx 1$ eV) and the adsorption saturation time of 10 s (upper bound, $E_{ads} \approx 0.8$ eV) from Ref. [16], the net 0.2 eV allows one to calculate occupancies. Note that in Ref. [13], the calculation for two competing species yielded the result of about $\theta_{O_2} = 89.3$ % and $\theta_{H_2O} = 10.7$ %.

If it is assumed that the partial pressure at each time is held constant, then the following occupancies serve as a lower bound estimate given the saturation of NO_3. At 200 s, the expected steady state occupancies are: $\theta_{O_2} = 84.4$ %, $\theta_{H_2O} = 10.1$ %, and $\theta_{NO_3} = 5.5$ %. At 1000 s, the resulting occupancies are: $\theta_{O_2} = 89.0$ %, $\theta_{H_2O} = 10.7$ %, and $\theta_{NO_3} = 0.3$ %. Lastly, at 8000 s, the results are: $\theta_{O_2} = 89.2$ %, $\theta_{H_2O} = 10.7$ %, and $\theta_{NO_3} = 0.1$ %. This behavior is consistent with the case of two competing species since NO_3 is not a significant atmospheric constituent. This analysis also shows that water remains a dominant desorbing agent for longer timescales, giving additional confirmation that $\tau_{NO_3} \approx 2575$ s ± 326 s under standard atmospheric

conditions. It should be noted that although similar desorption experiments may be performed in conditions where only a single species of gas is present, the timescale would likely be different due to the partial pressures being different than in atmospheric conditions. However, replicating laboratory settings necessitates analyzing data with several gas species that compete.

B. Numerical Verification of the Decay Models

To better justify the previous notion of using a three-term model for all analyses, a numerical analysis was performed for each fit to the experimental data, using a two-term, three-term, and four-term exponential decay (for a closer look at the reduced chi-squared comparison of single-, double-, and triple-term exponential decays, as well as all fits for Fig. 3 (d), see the Supplemental Material [46]). In this context, the use of the Bayes factor will better quantify the suitability of each of the exponential decay fits [56, 57].

The analysis begins by defining the marginal likelihood integral (MLI), where n is the number of parameters, L_{max} is the maximum likelihood [57], $\mathbf{Cov_p}$ is the parameter covariance matrix, and Δp is the parameter value range [56]:

$$MLI = (2\pi)^{n/2} L_{max} \frac{\sqrt{det\ \mathbf{Cov_p}}}{\prod_{i=1}^{n} \Delta p_i} \tag{6}$$

This metric characterizes a single fit to its corresponding dataset, and the Bayes factor emerges when the ratio between the MLIs for two different models is taken [56]. Typically, the Bayes factor assesses the quality of the model characterized in the numerator of the ratio relative to the model characterized in the denominator of the ratio. Therefore, the goal is to assess the three-term model with respect to the two-term model, bearing in mind that a Bayes factor over 100 (or,

alternatively for large datasets, a logarithm of the Bayes factor greater than 5) is an indication that the model of interest (three-term model) is quantifiably better than the model to which it is compared (two-term model). A Bayes factor closer to 1 indicates poor justification for using the model of interest. To provide an example evaluation of Eq. 6, the data from Fig. 3 (b) are used (red circles) here along with a two-term exponential decay fit: $n_h = y_0 + A_1 e^{-t/\tau_1} + A_2 e^{-t/\tau_2}$. The statistical quantities not directly involved in this analysis are provided in Fig. 1-SM (b) [46]. The corresponding covariance matrix output is the following (where each column in this symmetric matrix is designated by the fitting parameters y_0, A_1, τ_1, A_2, and τ_2, respectively):

$$\begin{pmatrix} 5.5 \times 10^{17} & -5.9 \times 10^{17} & -2.4 \times 10^{9} & 1.67 \times 10^{17} & -4.2 \times 10^{10} \\ -5.9 \times 10^{17} & 1.2 \times 10^{18} & 2.7 \times 10^{9} & -4.1 \times 10^{17} & 5.1 \times 10^{10} \\ -2.4 \times 10^{9} & 2.7 \times 10^{9} & 24 & -2.5 \times 10^{9} & 217.9 \\ 1.67 \times 10^{17} & -4.1 \times 10^{17} & -2.5 \times 10^{9} & 4.1 \times 10^{17} & -2.1 \times 10^{10} \\ -4.2 \times 10^{10} & 5.1 \times 10^{10} & 217.9 & -2.1 \times 10^{10} & 3440.6 \end{pmatrix}$$

Above, $\sqrt{det\ \mathbf{Cov_p}}$ can be determined numerically (for this two-term example, the value is on the order of 10^{27}), n is 5, and $\prod_{i=1}^{n} \Delta p_i$ is approximately on the order of 10^{45}. The latter is based on each coefficient of carrier density having a range up to about 10^{12} cm^{-2} and the two time-based parameters given a range up to 10^4 s. Though the technical unit for the value in this example is s^2·cm^{-6}, it will change based on the model of interest, as will the unit for $\sqrt{det\ \mathbf{Cov_p}}$. The final factor, L_{max}, was calculated by the exact means outlined in [56], and, in summary, involves calculating the probability distribution function (PDF) of the dataset. Due to the large number of data points, it is more helpful to compute its logarithm, resulting in $log\ (L_{max})$ being approximately 1620 for the two-term model.

By repeating this rigorous analysis to each model for each dataset, it is found that the *logarithm* of the Bayes factor comparing the three-term model to the two-term model is much

greater than 5 (and thus, the Bayes factor itself much greater than 100), indicating that the former is a decisively stronger model to use.

The final question remaining involves repeating this entire Bayes factor analysis for the case where the four-term model is compared to the three-term model. Despite having a better reduced chi-squared, the four-term model fails to meet the Bayes criterion for justifying its use. For example, by using the same data from Fig. 3 (b) (red circles), it is found that the ratio of the MLIs, with the four-term model as the numerator, was a positive number much smaller than 1 (and a logarithm on the order of -10^2), indicating that the two additional parameters (nominally A_4 and τ_4) were not relevant from a statistical perspective.

C. Monitoring the 2D (G') Raman Mode

Supporting evidence of the inherent timescales associated with this transient hole doping was collected via Raman spectroscopy performed on functionalized devices. Local joule heating was not considered due to the high heat conductivity of both EG and the SiC substrate [58]. After collecting a time series of Raman spectra, examples of which are shown in Fig. 4 (a), the 2D (G') mode frequencies required analysis. The four example spectra were observed at four distinct times labeled t_1 through t_4 and correspond to 0 s, 5×10^3 s, 10^4 s, and 1.2×10^4 s, respectively. The peaks at all times were fit to a Lorentzian profile to extract the frequency. The fitting results are shown in Fig. 4 (c) as black data points with error bars indicating 1σ error from the peak fitting procedure. The issue now becomes how to determine the relationship between the 2D mode frequency and n_h, and two analyses were conducted to understand this relationship.

The first analysis involves using the existing literature to calculate an expected behavior of the 2D mode frequency with time. To accomplish this, a best-fit cubic curve was used (extracted from Ref. [58], shown by the inset of Fig. 4 (b)). This curve relating Fermi energy and 2D mode

frequency was recalculated to instead show the relationship between the 2D mode frequency and n_h via $E_F = \hbar v_F \sqrt{\pi |n_h|} sign(n_h)$. This recalculation used two known conditions: (1) n_h was determined by electrical transport and was predictable (about 1.1 × 10^{12} cm^{-2}), and (2) n_h could be approximated at the minimum wavenumber as corresponding to the Dirac point given the results of Fig. 3 (c). Using this recalculation, average time-dependent n_h curves were transformed to calculate a predicted Raman peak shifting (gold) based on the time constants acquired with transport in Fig. 4 (c). The dashed cyan curves are repeated calculations based on different time constants to show the extent of the prediction accuracy.

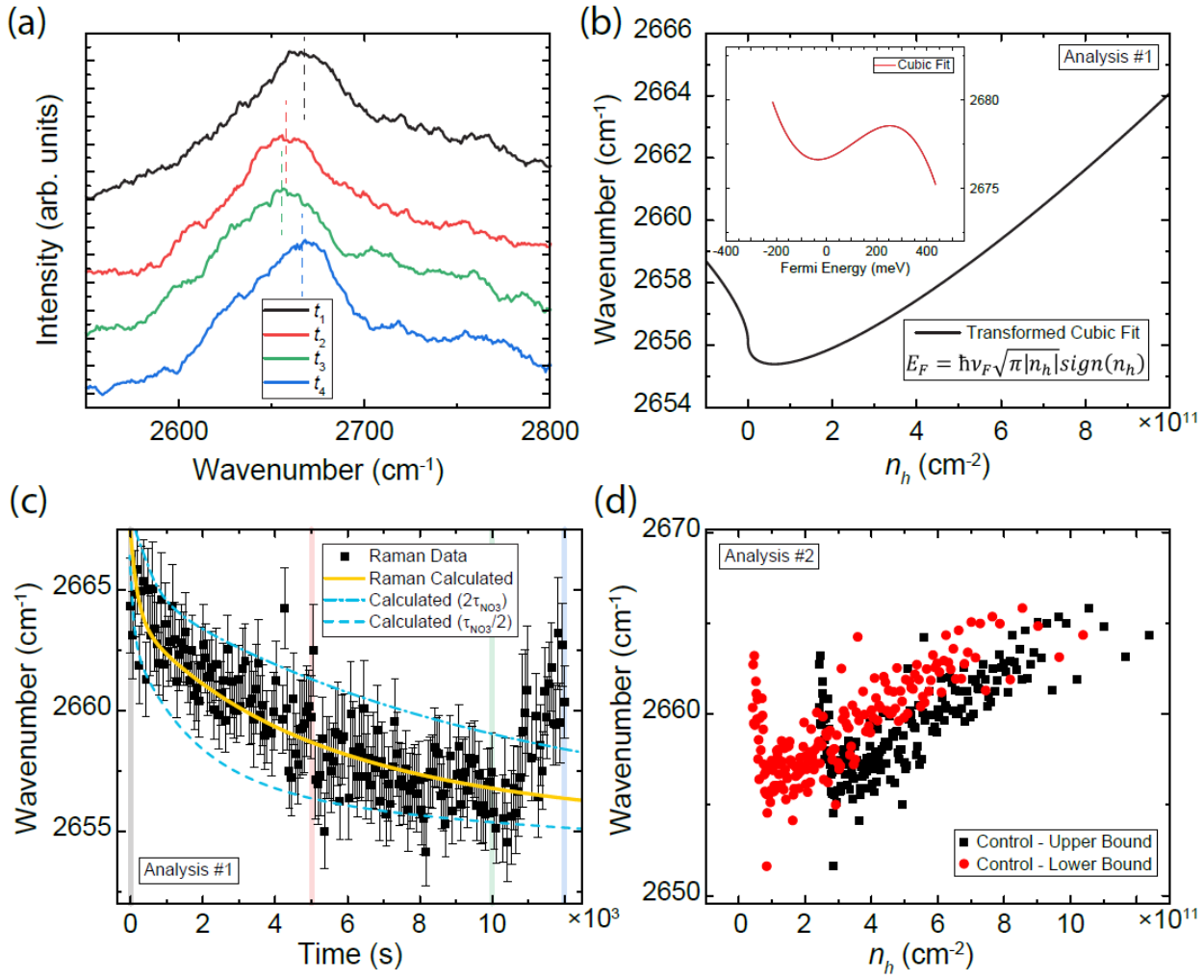

FIG. 4. (Color online) Spectroscopic verification of observed time constants. (a) Example Raman spectra focused on the 2D (G′) mode of EG. These four spectra are observed at four distinct times labeled t_1 through t_4 and correspond to 0 s, 5×10^3 s, 10^4 s, and 1.2×10^4 s, respectively. (b) The relationship between the 2D mode frequency and n_h is calculated by using a best-fit cubic curve as extracted from Ref. [58] (inset, which notes the 2D mode frequency as a function of Fermi energy). For this first analysis, this transformation is given two initial conditions: the first n_h is known and n_h is known at the minimum wavenumber (corresponding to the Dirac point). (c) The 2D mode frequencies for the time series measurements are plotted (with error bars indicating 1σ error from the peak fitting procedure). Calculated trends of the Raman peak shifting are plotted in gold (solid) and cyan (dashed) based on the relevant time constant. Four thin, color-matched bands mark the same times listed in (a). (d) A second analysis reveals a relationship between the 2D mode frequency and n_h as extracted from the data directly, with the mode's doping-dependence showing reasonable behavior when compared to the literature.

It should be noted that the prediction of the Raman trend (gold curve) is a simple transformation that gives a 1:1 correspondence between 2D mode frequency and n_h. The immediate rise in wavenumber that occurs after the minimum can be attributed to the change in polarity of the charge carrier. It behaves reasonably considering that a similar trend can be seen in Fig. 4 (b) as one considers crossing the Dirac point to obtain an electron density (or below $n_h \approx 0$ cm^{-2}).

For the second analysis, one may decide to forego the use of predictive assistance from the literature. The alternate approach would be to use the time-dependent n_h curve as a direct method to reveal the relationship between the 2D mode frequency and n_h. On the one hand, the mode's doping-dependence, shown in Fig. 4 (d) for an example control device, shows a reasonable behavior when compared to the literature [59-60]. The major issue that arises from this alternate approach is that the wavenumber extrema appear to occur at some arbitrary positive value of n_h.

This horizontal departure from the calculation in Fig. 4 (b) demonstrates that, especially

for devices with more variation in n_h, an unexplainable minimum can arise in the final transformed data. That said, some of the error could be accounted for by means of introducing a rigorous horizontal error bar, but this ultimately reduces the predictive quality between a device's hole doping and the frequency of its 2D mode. And though this analysis should not be a primary method for narrowly predicting the hole density in EG, the Raman data may easily be mathematically transformed to appear like the inset of Fig. 4 (b). Thus, the data provide direct experimental evidence for the nuanced relationship between the Fermi energy and the corresponding Raman shift in EG on 4H-SiC.

V. CONCLUSIONS

In this work, the dynamics of transient hole doping are reported for epitaxial graphene devices that are both untreated and functionalized. Nitric acid was used as the adsorbent, and corresponding timescales associated with its desorption were determined from transport and electrical monitoring data. The understanding of reversible hole doping without gating is of crucial importance to those seeking to fabricate devices on length scales where metallic gating becomes unfeasible. Optical properties were also monitored with time after exposure via Raman spectroscopy, supporting the determined time constants for NO_3. These results will be relevant for future device fabrication involving any material that can be hole (or electron) doped by chemical means.

ACKNOWLEDGMENTS AND NOTES

The authors thank L. S. Chao, A. L. Levy, G. J. Fitzpatrick, and E. C. Benck for their assistance with the NIST internal review process. Work presented herein was performed, for a subset of the

authors, as part of their official duties for the United States Government. Funding is hence appropriated by the United States Congress directly. The authors declare no competing interest.

Commercial equipment, instruments, and materials are identified in this paper in order to specify the experimental procedure adequately. Such identification is not intended to imply recommendation or endorsement by the National Institute of Standards and Technology or the United States Government, nor is it intended to imply that the materials or equipment identified are necessarily the best available for the purpose.

REFERENCES

[1] A.K. Geim and K.S. Novoselov, Nat. Mater. **6**, 183 (2007).

[2] A.H. Castro Neto, F. Guinea, N. M. R. Peres, K. S. Novoselov, and A. K. Geim, Rev. Mod. Phys. **81**, 109 (2009).

[3] K.S. Novoselov, V.I. Fal'ko, L. Colombo, P.R. Gellert, M.G. Schwab, and K. A. Kim, Nature **490**, 192 (2012).

[4] S. Das Sarma, S. Adam, E.H. Hwang, and E. Rossi, Rev. Mod. Phys. **83**, 407 (2011).

[5] T. Oe, A. F. Rigosi, M. Kruskopf, B. Y. Wu, H. Y. Lee, Y. Yang, R. E. Elmquist, N. H. Kaneko, D. G. Jarrett, IEEE Trans. Instrum. Meas. **69**, 3103-8 (2019).

[6] A. Tzalenchuk, S. Lara-Avila, A. Kalaboukhov, S. Paolillo, M. Syväjärvi, R. Yakimova, O. Kazakova, T.J.B.M. Janssen, V. Fal'ko, and S. Kubatkin, Nat Nanotechnol. 5, **186** (2010).

[7] A. F. Rigosi, R. E. Elmquist, Semicond. Sci. Technol. **34**, 093004 (2019).

[8] F. Lafont, R. Ribeiro-Palau, D. Kazazis, A. Michon, O. Couturaud, C. Consejo, T. Chassagne, M. Zielinski, M. Portail, B. Jouault, F. Schopfer, W. Poirer, Nat. Commun. **6**, 6806 (2015).

[9] A. F. Rigosi, N. R. Glavin, C.-I. Liu, Y. Yang, J. Obrzut, H. M. Hill, J. Hu, H.-Y. Lee, A. R. Hight Walker, C. A. Richter, R. E. Elmquist, and D. B. Newell, Small **13**, 1700452 (2017).

[10] M. Kruskopf, A. F. Rigosi, A. R. Panna, M. Marzano, D. Patel, H. Jin, D. B. Newell, and R. E. Elmquist, Metrologia **56**, 065002 (2019).

[11] R. Ribeiro-Palau, F. Lafont, J. Brun-Picard, D. Kazazis, A. Michon, F. Cheynis, O. Couturaud, C. Consejo, B. Jouault, W. Poirier, and F. Schopfer, Nat. Nanotechnol. **10**, 965 (2015).

[12] H. He, K. H. Kim, A. Danilov, D. Montemurro, L. Yu, Y. W. Park, F. Lombardi, T. Bauch, K. Moth-Poulsen, T. Iakimov, and R. Yakimova, Nat. Commun. **9**, 3956 (2018).

[13] A.F. Rigosi, M. Kruskopf, H.M. Hill, H. Jin, B.-Y. Wu, P.E. Johnson, S. Zhang, M. Berilla, A.R. Hight Walker, C.A. Hacker, D.B. Newell, and R.E. Elmquist, Carbon **142**, 468 (2019).

[14] A. Lartsev, T. Yager, T. Bergsten, A. Tzalenchuk, T. M. Janssen, R. Yakimova, S. Lara-Avila, S. Kubatkin. Appl. Phys. Lett. **105**, 063106 (2014).

[15] F. Gunes, H. Arezki, D. Pierucci, D. Alamarguy, J. Alvarez, J.-P. Kleider, Y. J. Dappe, A. Ouerghi, and M. Boutchich, Nanotechnol. **26**, 445702 (2015).

[16] L. D'Arsie, S. Esconjauregui, R. S. Weatherup, X. Wu, W. E. Arter, H. Sugime, C. Cepek, and J. Robertson, RSC Adv. **6**, 113185 (2016).

[17] A. Kasry, M. A. Kuroda, G. J. Martyna, G. S. Tulevski and A. A. Bol, ACS Nano **4**, 3839–3844 (2010).

[18] J.-M. Yun, Y.-J. Noh, J.-S. Yeo, Y.-J. Go, S.-I. Na, H.-G. Jeong, J. Kim, S. Lee, S.-S. Kim, H. Y. Koo, T.-W. Kim and D.-Y. Kim, J. Mater. Chem. C **1**, 3777–3783 (2013).

[19] Z. Liu, S. P. Lau, and F. Yan, Chem. Soc. Rev. **44**, 5638 (2015).

[20] M. Yoshida, Y. Zhang, J. Ye, R. Suzuki, Y. Imai, S. Kimura, A. Fujiwara, and Y. Iwasa, Sci. Rep. **4**, 7302 (2014).

[21] H. M. Hill, S. Chowdhury, J. R. Simpson, A. F. Rigosi, D. B. Newell, H. Berger, F. Tavazza, and A. R. Hight Walker, Phys. Rev. B **99**, 174110 (2019).

[22] J. Hu, A. F. Rigosi, M. Kruskopf, Y. Yang, B. Y. Wu, J. Tian, *et al.* Sci. Rep., **8**, 1-11 (2018).

[23] A. F. Rigosi, D. Patel, M. Marzano, M. Kruskopf, H. M. Hill, H. Jin, J. Hu, A. R. Hight Walker, M. Ortolano, L. Callegaro, C.-T. Liang, and D. B. Newell, Carbon **154**, 230 (2019).

[24] B. Huard, J. A. Sulpizio, N. Stander, K. Todd, B. Yang, and D. Goldhaber-Gordon, Phys. Rev. Lett. **98**, 236803 (2007).

[25] J. Hu, A. F. Rigosi, J. U. Lee, H.-Y. Lee, Y. Yang, C.-I Liu, R. E. Elmquist, and D. B. Newell, Phys. Rev. B **98**, 045412 (2018).

[26] H. Schmidt, J. C. Rode, C. Belke, D. Smirnov, and R. J. Haug, Phys. Rev. B **88**, 075418 (2013).

[27] A. F. Rigosi, M. Marzano, A. Levy, H. M. Hill, D. K. Patel, M. Kruskopf, H. Jin, R. E. Elmquist, and D. B. Newell, Physica B **582**, 411971 (2020).

[28] X. Gan, R.-J. Shiue, Y. Gao, I. Meric, T. F. Heinz, K. Shepard, J. Hone, S. Assefa, and D. Englund, Nat. Photonics **7**, 883 (2013).

[29] F. Xia, T. Mueller, Y. Lin, A. Valdes-Garcia, and P. Avouris, Nat. Nanotechnol. **4**, 839 (2009).

[30] T. Mueller, F. Xia, and P. Avouris, Nat. Photonics **4**, 297 (2010).

[31] S. Schuler, D. Schall, D. Neumaier, L. Dobusch, O. Bethge, B. Schwarz, M. Krall, and T. Mueller, Nano Lett. **16**, 7107 (2016).

[32] J. Fang, D. Wang, C. T. DeVault, T.-F. Chung, Y. P. Chen, A. Boltasseva, V. M. Shalaev, and A. V. Kildishev, Nano Lett. **17**, 57 (2017).

[33] S. Chen, Z. Han, M. M. Elahi, K. M. Masum Habib, L. Wang, B. Wen, Y. Gao, T. Taniguchi, K. Watanabe, J. Hone, A. W. Ghosh, and C. R. Dean, Science **353**, 1522 (2016).

[34] R. N. Sajjad and A. W. Ghosh, Appl. Phys. Lett., **99**, 123101 (2011).

[35] M. M. Elahi, K. M. Masum Habib, K. Wang, G.-H. Lee, P. Kim, and A. W. Ghosh, Appl. Phys. Lett. **114,** 013507 (2019).

[36] T. Seyller, A. Bostwick, K. V. Emtsev, K. Horn, L. Ley, J. L. McChesney, T. Ohta, J. D. Riley, E. Rotenberg, F. Speck, Phys. Status Solidi (b) **245**, 1436-46 (2008).

[37] M. Kruskopf, D. M. Pakdehi, K. Pierz, S. Wundrack, R. Stosch, T. Dziomba, *et al*. 2D Mater. **3**, 041002 (2016).

[38] A. F. Rigosi, H. M. Hill, N. R. Glavin, S. J. Pookpanratana, Y. Yang, A. G. Boosalis, J. Hu, A. Rice, A. A. Allerman, N. V. Nguyen, C. A. Hacker, R. E. Elmquist, A. R. Hight Walker, and D. B. Newell, 2D Mater. **5**, 011011 (2017).

[39] A. F. Rigosi, C.-I. Liu, B.-Y. Wu, H.-Y. Lee, M. Kruskopf, Y. Yang, H. M. Hill, J. Hu, E. G. Bittle, J. Obrzut, A. R. Hight Walker, R. E. Elmquist, and D. B. Newell, Microelectron. Eng. **194**, 51-5 (2018).

[40] M. Kruskopf, A. F. Rigosi, A. R. Panna, D. K. Patel, H. Jin, M. Marzano, M. Berilla, D. B. Newell, and R. E. Elmquist, IEEE Trans. Electron Dev. **66**, 3973 (2019).

[41] E. Bekyarova, S. Sarkar, S. Niyogi, M.E. Itkis, and R.C. Haddon, J. Phys. D: Appl. Phys. **45**, 154009 (2012).

[42] T. J. B. M. Janssen, A. Tzalenchuk, R. Yakimova, S. Kubatkin, S. Lara-Avila, S. Kopylov, et al. Phys. Rev. B **83**, 233402 (2011).

[43] H. M. Hill, A. F. Rigosi, S. Chowdhury, Y. Yang, N. V. Nguyen, F. Tavazza, R. E. Elmquist, D. B. Newell, and A. R. Hight Walker, Phys. Rev. B **96**, 195437 (2017).

[44] S. Weingart, C. Bock, U. Kunze, K. V. Emtsev, Th. Seyller, and L. Ley, Physica E **42**, 687-690 (2010).

[45] N. J. G. Couto, D. Costanzo, S. Engels, D.-K. Ki, K. Watanabe, T. Taniguchi, C. Stampfer, F. Guinea, A. F. Morpurgo, Phys. Rev. X **4**, 041019 (2014).

[46] See Supplemental Material at [URL] for the exponential decay analysis, demonstration of fits, and information on dopant interactions on the EG surface. This includes References [61-63].

[47] P. D. Kaushik, M. Rodner, G. B. V. S. Lakshmi, I. G. Ivanov, G. Greczynski, J. Palisaitis, J. Eriksson, P. Solanki, A. Aziz, A. M. Siddiqui, R. Yakimova, M. Syvajarvi, and G. R. Yazdi, Carbon **157**, 169-184 (2020).

[48] Md. W. K. Nomani, R. Shishir, M. Qazi, D. Diwan, V. B. Shields, M. G. Spencer, G. S. Tompa, N. M. Sbrockey, and G. Koley, Sens. Actuators B Chem. **150**, 301-307 (2010).

[49] C. Melios, C.E. Giusca, V. Panchal, and O. Kazakova, 2D Mater. **5**, 022001 (2018).

[50] F.R. Bagsican, A. Winchester, S. Ghosh, X. Zhang, L. Ma, M. Wang, H. Murakami, S. Talapatra, R. Vajtai, P.M. Ajayan, J. Kono, M. Tonouchi, and I. Kawayama, Sci. Rep., 7 (2017), pp. 1774-1-1774-10.

[51] S. Bottcher, H. Vita, M. Weser, F. Bisti, Y.S. Dedkov, and K. Horn, J. Phys. Chem. Lett., 8 (2017), pp. 3668-3672.

[52] I. Silvestre, E.A. de Morais, A.O. Melo, L.C. Campos, A.-M.B. Goncalves, A.R. Cadore, *et al.*, ACS Nano **7**, 6597-6604 (2013).

[53] F. Yavari, C. Kritzinger, C. Gaire, L. Song, H. Gullapalli, T. Borca-Tasciuc, *et al*., Small **6**, 2535-2538 (2010).

[54] K. Maier, A. Helwig, G. Muller, P. Hille, J. Teubert, M. Eickhoff, Sens. Actuator B., 250 (2017), pp. 91-99.

[55] E. L. Cussler, (1997). Diffusion: Mass Transfer in Fluid Systems (2nd ed.). New York: Cambridge University Press.

[56] D. J. Dunstan, J. Crowne, A. J. Drew, Sci. Rep. **12**, 993 (2022).

[57] D. J. C. MacKay, Neural Comput. **4**, 448 (1992).

[58] Y. Yue, J. Zhang, and X. Wang, Small **7**, 3324 (2011).

[59] G. Froehlicher and S. Berciaud, Phys. Rev. B **91**, 205413 (2015).

[60] A. Das, S. Pisana, B. Chakraborty, S. Piscanec, S. K. Saha, U. V. Waghmare, K. S. Novoselov, H. R. Krishnamurthy, A. K. Geim, A. C. Ferrari, and A. K. Sood, Nat. Nanotechnol. **3**, 210-215 (2008).

[61] O. Leenaerts, B. Partoens, and F. M. Peeters, Phys. Rev. B **77**, 125416 (2008).

[62] Z. Li, Y. Wang, A. Kozbial, G. Shenoy, F. Zhou, R. McGinley, P. Ireland, B. Morganstein, A. Kunkel, S. P. Surwade, L. Li, Nat. Mater. **12**, 925 (2013).

[63] C. N. Santos, F. Joucken, D. De Sousa Meneses, P. Echegut, J. Campos-Delgado, P. Louette, J.-P. Raskin, and B. Hackens, Sci. Rep. **6**, 24301 (2016).

Supplemental Material

Dynamics of Transient Hole Doping in Epitaxial Graphene

Swapnil M. Mhatre[1,2], Ngoc Thanh Mai Tran[1,3], Heather M. Hill[1], Dipanjan Saha[1], Angela R. Hight Walker[1], Chi-Te Liang[2], Randolph E. Elmquist[1], David B. Newell[1], and Albert F. Rigosi[1†]

[1]*Physical Measurement Laboratory, National Institute of Standards and Technology (NIST), Gaithersburg, MD 20899, United States*

[2]*Graduate Institute of Applied Physics, National Taiwan University, Taipei 10617, Taiwan*

[3]*Joint Quantum Institute, University of Maryland, College Park, Maryland 20742, United States*

Exponential Decay Analysis

Fig. 1-SM shows the analysis (based on Fig. 3 (b)) to justify why a three-term exponential decay was more optimal than either a single- or double-term decay. The two-term decay has a worse reduced chi-squared when compared with the three-term decays, and so one may also rely on the existing knowledge of physical desorption processes of other species (like water and oxygen) to make a clearer distinction between the two different fitting procedures, as well as the knowledge that NO_2 is present on the EG surface, as cited by the main text.

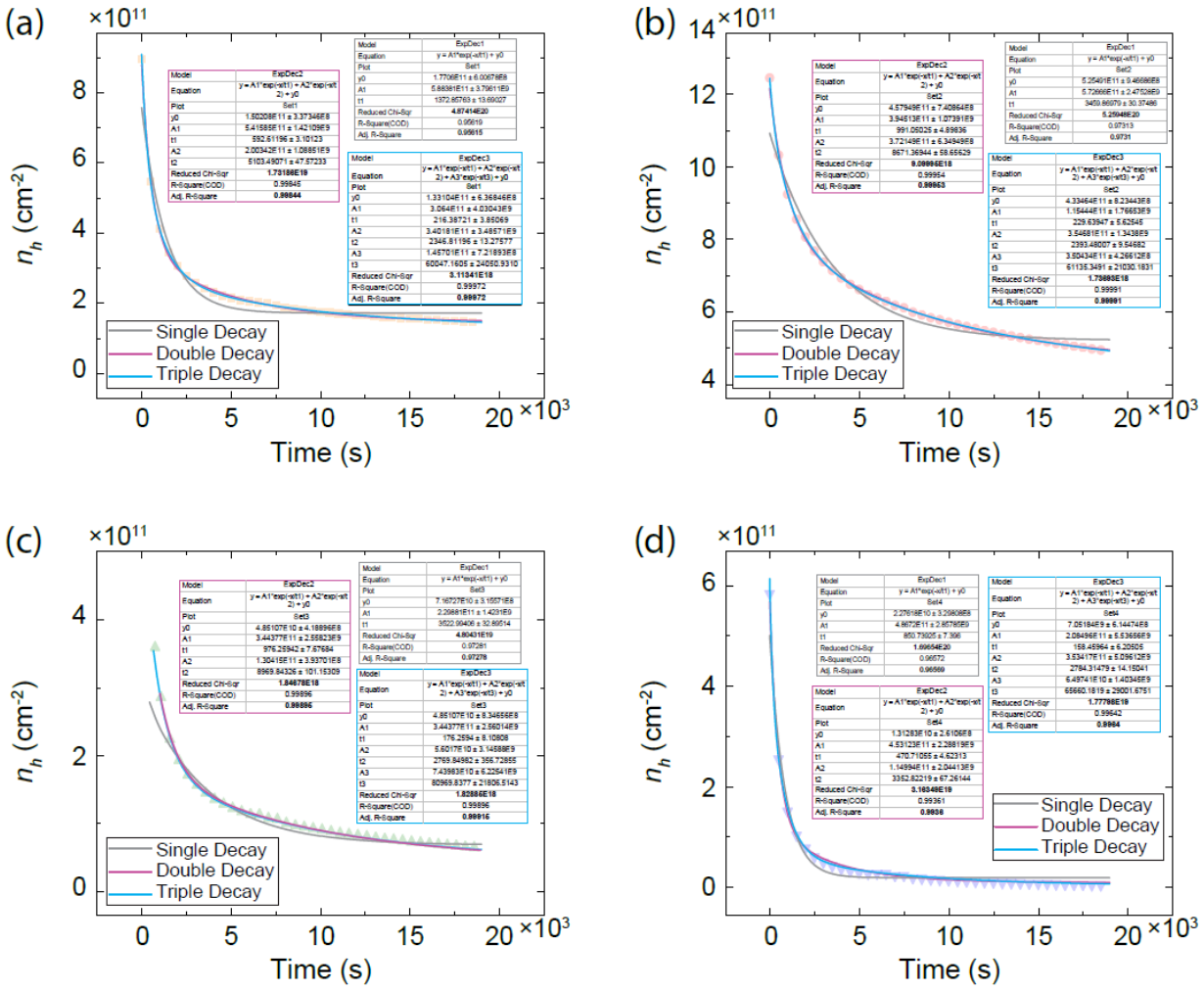

Figure 1-SM. Each Langmuir fit in the main text was used to transform the corresponding R_{xx} data to n_h. (a)-(d) Each time dependent n_h curve was fit to single-, double-, and triple-term exponential decay fits to verify the quality of the lattermost fit.

Demonstration of Fits

Fig. 2-SM shows all fits from Fig. 3 (d) to demonstrate the ability of extracting similar time constants. These data are just a subset of all data from control and functionalized devices.

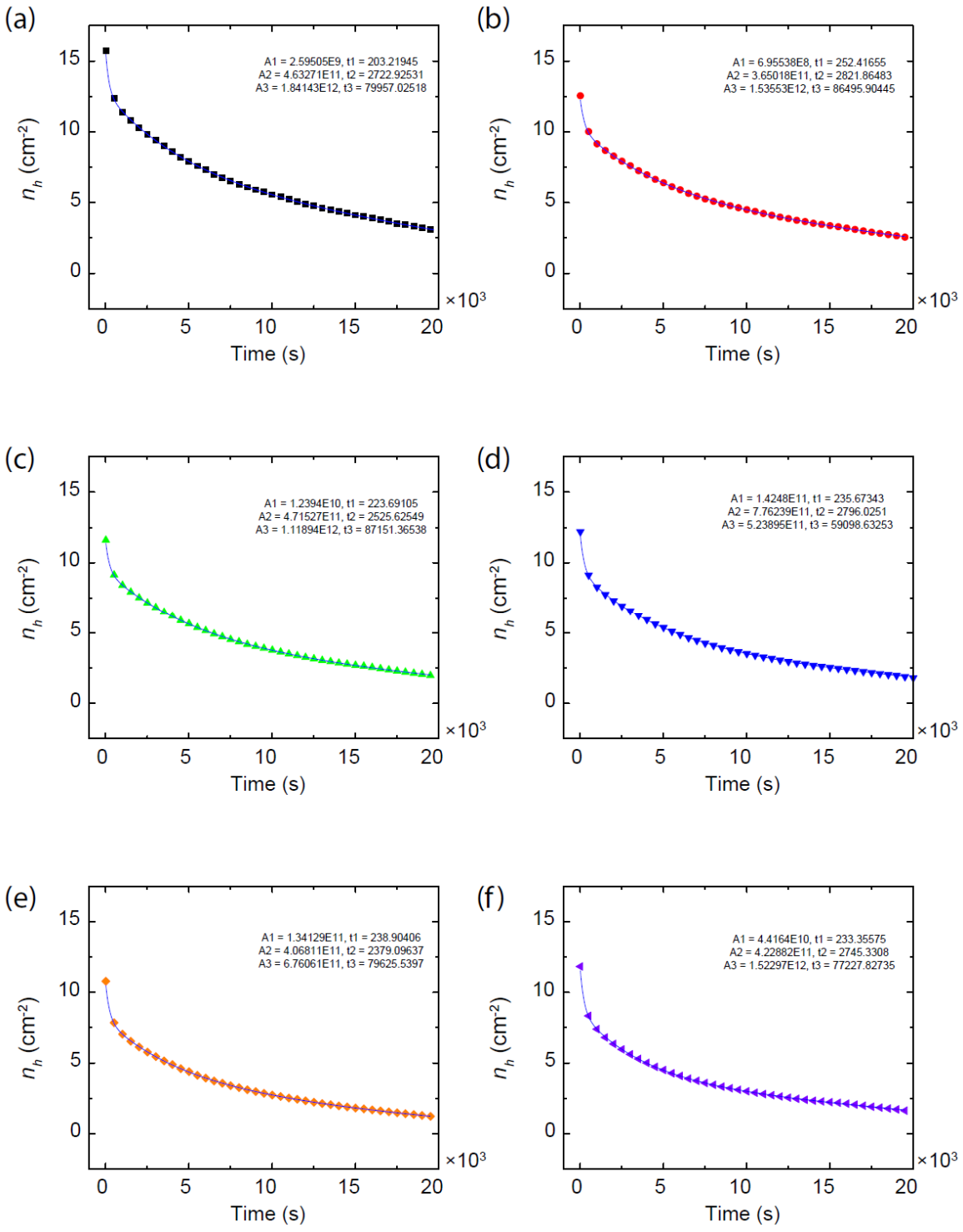

Figure 2-SM. Each curve from Fig. 3 (d) in the main text is fit to a triple-term exponential decay to extract the relevant time constants. These data are just a subset of all data collected from control and functionalized devices.

Illustration of Dopant Interactions

Theoretical calculations show that NO_2 is a stronger acceptor of electrons than H_2O by about a factor of 4 [1]. And given the relative similarity of H_2O and O_2 as acceptors on EG (when comparing their adsorption times and energies) [2-5], it is not unreasonable to posit NO_2 being a similarly strong acceptor when compared to O_2. Furthermore, the radicals NO_2 and NO_3 are calculated to be of similar strength in terms of electron transfer from EG [6]. On a similar note, some works report on the influence of hydrocarbons when discussing desorption or adsorption processes on graphene [7]. It should be noted that under most conditions, if a molecule does not exert a partial pressure in the total volume of its environment, it will desorb. That said, the case of Ref. [7] offers an interesting point for graphene grown by chemical vapor deposition, where it observes a signature of CH_2 in a spectrum taken with Fourier transform infrared spectroscopy after 10 min in air. We posit that due to the growth technique, it is possible that the CVD graphene has been prone to adsorbing precursor material that may have lingered on the surface. The claim that EG is less likely to exhibit this behavior can be substantiated by other EG observations using FTIR, while noticing that the CH_2 signature no longer appears [8].

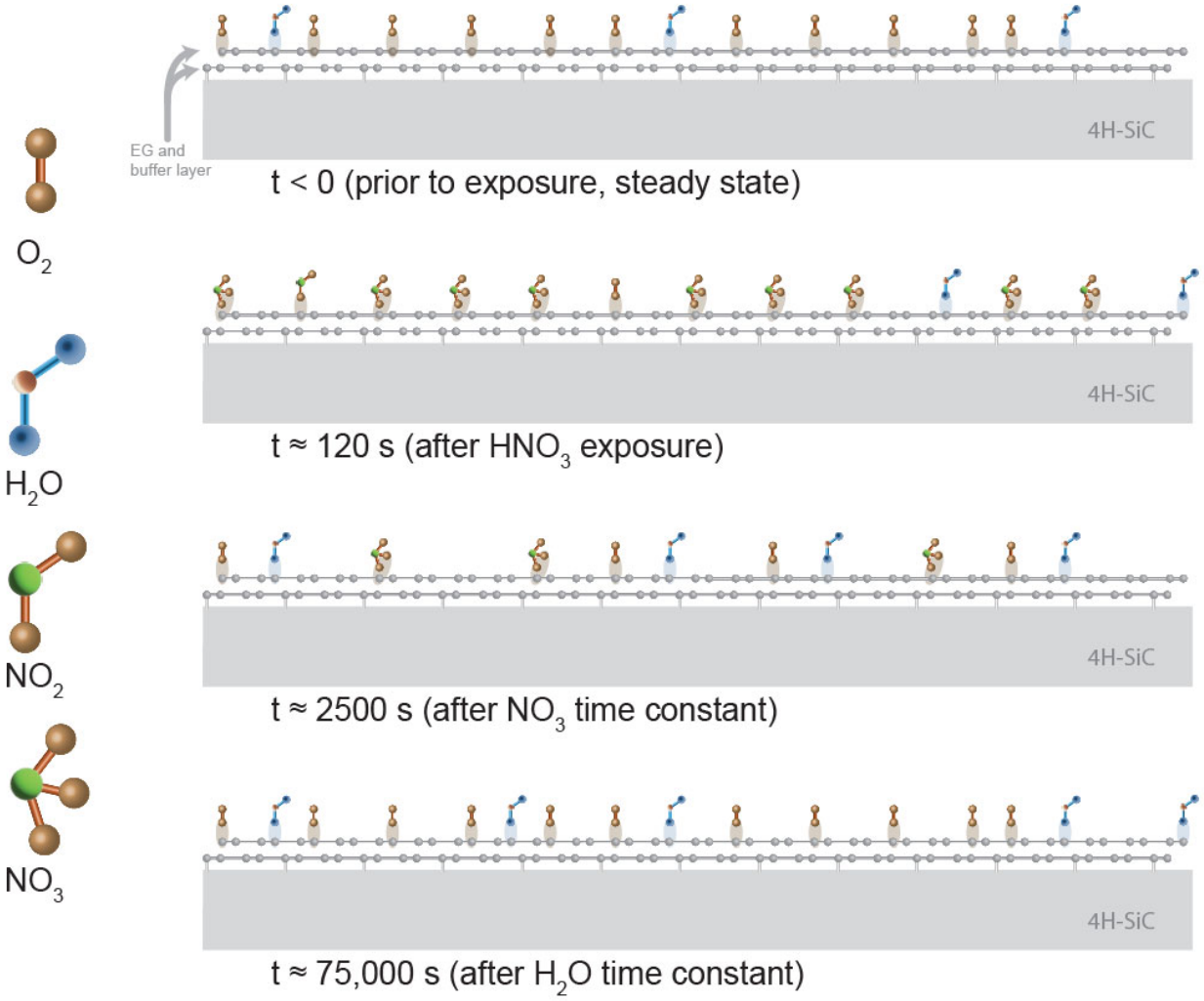

Figure 3-SM. Illustrations of possible configurations of surface coverage are provided here at various points of the desorption process. This figure is meant to guide intuition and is not a precise rendering or scaling of the system.

REFERENCES

[1] O. Leenaerts, B. Partoens, and F. M. Peeters, Phys. Rev. B **77**, 125416 (2008).

[2] C. Melios, C.E. Giusca, V. Panchal, and O. Kazakova, 2D Mater. **5**, 022001 (2018).

[3] F.R. Bagsican, A. Winchester, S. Ghosh, X. Zhang, L. Ma, M. Wang, H. Murakami, S. Talapatra, R. Vajtai, P.M. Ajayan, J. Kono, M. Tonouchi, and I. Kawayama, Sci. Rep., 7 (2017), pp. 1774-1-1774-10.

[4] S. Bottcher, H. Vita, M. Weser, F. Bisti, Y.S. Dedkov, and K. Horn, J. Phys. Chem. Lett., 8 (2017), pp. 3668-3672.

[5] I. Silvestre, E.A. de Morais, A.O. Melo, L.C. Campos, A.-M.B. Goncalves, A.R. Cadore, *et al.*, ACS Nano **7**, 6597-6604 (2013).

[6] L. D'Arsie, S. Esconjauregui, R. S. Weatherup, X. Wu, W. E. Arter, H. Sugime, C. Cepek, and J. Robertson, RSC Adv. **6**, 113185 (2016).

[7] Z. Li, Y. Wang, A. Kozbial, G. Shenoy, F. Zhou, R. McGinley, P. Ireland, B. Morganstein, A. Kunkel, S. P. Surwade, L. Li, Nat. Mater. **12**, 925 (2013).

[8] C. N. Santos, F. Joucken, D. De Sousa Meneses, P. Echegut, J. Campos-Delgado, P. Louette, J.-P. Raskin, and B. Hackens, Sci. Rep. **6**, 24301 (2016).